

Topological properties of a periodically driven Creutz ladder

Koustav Roy and Saurabh Basu

Department of Physics, Indian Institute of Technology Guwahati-Guwahati, 781039 Assam, India

(Received 7 February 2023; accepted 10 July 2023; published 24 July 2023)

We have investigated a periodically driven Creutz ladder in the presence of two different driving protocols, namely, a sinusoidal drive and a δ kick imparted to the ladder at regular intervals of time. Specifically, we have studied the topological properties corresponding to the trivial and the nontrivial limits of the static (undriven) case via computing suitable topological invariants. Corresponding to the case where the chiral symmetry of the ladder is intact, in addition to the zero energy modes, π energy modes appear in both these cases. Further, two different frequency regimes of the driving protocol emerge, where the Floquet-Magnus expansion is employed particularly to study the high-frequency regime for the sinusoidal drive. Apart from the physics being identical in the high-frequency and the static scenarios, the zero energy modes show distinctive features at low and high frequencies. For the sinusoidal drive, there exists a sharp frequency threshold beyond which the zero energy modes only exist in the topological limit, while in the trivial limit, it exist only up to the same threshold frequency. In presence of the δ kick, the Creutz ladder demonstrates higher values of the topological invariant, and as a consequence, the system possesses a larger number of edge modes.

DOI: [10.1103/PhysRevB.108.045415](https://doi.org/10.1103/PhysRevB.108.045415)**I. INTRODUCTION**

Topological insulators are materials that exhibit bulk states which are gapped, similar to a conventional insulator, whereas the states at the boundaries are gapless. These states contribute to the electronic transport properties. The presence of these localized boundary states is solely determined by the bulk properties of the system (“bulk-edge correspondence”), and they are immune to local perturbations that do not close the spectral gap and hence allow for nondissipative electronic transport [1–5]. The Creutz ladder is an example of such a material having quasi-1D structure and consists of two rungs of lattice sites that are coupled by diagonal, vertical, and horizontal hoppings. Additionally, a magnetic flux can penetrate the ladder perpendicularly to its plane, giving access to an extra degree of freedom in the form of the Peierls phase [6–8], associated with the horizontal hopping amplitude. Moreover, the localization of the zero energy modes is also characterized in terms of Aharonov-Bohm caging. Due to this dual protection (Aharonov-Bohm caging and topological symmetry conservation), the edge modes are very robust irrespective of the system size. These intriguing properties may make the Creutz ladder a promising candidate for different applications in high-performance electronics and quantum computing.

The dynamics of quantum systems is another topic of considerable interest, and is actively explored in the field of topology. Recent studies have established that applying external periodic drives can open a route to engineer topological nontriviality with high tunability from materials that are even topologically trivial in equilibrium [9–12]. Furthermore, because of the periodicity in time, the energy bands are folded back to a Floquet Brillouin zone (FBZ), at the boundary of which a new variety of edge modes, namely, the so called π modes, appear. The value of the topological invariants, predicting the number of the zero and the π quasienergy

end states, can be controlled by the parameters, such as frequency and amplitude of the drive. In general, the Floquet topological insulators (FTIs) show rich topological phases that may not have any analogy with the undriven case. Examples include generation of higher Chern numbers in a 1D extended Su-Schrieffer-Heeger (E-SSH) model [13,14], and some other 2D models [15,16], emergence of the time crystalline phase along with period doubling oscillations in 1D time Floquet SSH models [17,18], rich entanglement properties of the time-periodic Kitaev chain [19–21], and Floquet analysis of higher-order topological insulators [22–25]. These works have continued to draw attention from the community owing to the experimental success in driving quantum systems. For example, the experimental realization of FTIs is done on a nanophotonics platform using a lattice of strongly coupled octagonal resonators in the silicon-on-insulator material system [26]. Further, the time periodicity of any system may be exploited by the means of photoinduced band gaps, which further can be resolved by the technique called time and angle resolved photoemission spectroscopy (t-ARPES) [27,28].

The application of Floquet dynamics is well explored in the field of 1D topological insulators, like the SSH chain or Kitaev chain with p -wave superconductivity [29–32]. Among other systems, Floquet topological characterization of some chaotic models [33–35], for example, a kicked Harper model, on-resonance double-kicked rotor model [36,37], etc., have unveiled interesting features. Recent work [38] has suggested that the mechanism of the two seemingly disparate topics of chaotic behavior and topology may have a one-to-one correspondence. Further, studies on several nonequilibrium quantities for chiral ladder networks have emerged as an active field of research [39,40]. This intrigues the fundamental interest in quest of a richer variety of topological properties in time-periodic 1D models with a nominal quasi-one-dimensionality. In this context, the Creutz

ladder denotes a paradigmatic model, owing to its experimental realizability in cold-atomic systems [41–43]. Unlike the generic 1D topological insulators, due to the presence of magnetic-flux-dependent chiral symmetry and the (controversial) time-reversal symmetry [39,44], it is hard to place the model in the Altland-Zirnbauer (AZ) classification scheme [45]. Interestingly, ladder networks of the Creutz family are very useful in unveiling important two-dimensional topological aspects and symmetry classification schemes owing to their apparent quasi-1D nature [3]. Moreover, the Aharonov-Bohm caging effect leads to destructive quantum interference that impedes the motion of the particles. As a result, one gets perfectly localized energy modes, a special property of flat band networks [8,46]. Recent investigations propose various modified versions of the Creutz ladder, which reflects rich information in the field of localization dynamics [47,48], many-body interactions [44], etc.

In this work, we shall highlight the Floquet aspects captured by the ladder when the hopping amplitudes are modulated in time by two different driving protocols, namely, (a) a sinusoidal drive and (b) a δ kick. We shall also provide a comparison between the two protocols and the corresponding insights induced by them. In a generic sense, these two drives account for any kind of periodically driven system. Our primary goal is here to compare and contrast time-independent Floquet Hamiltonians, constructed from these two drives.

The layout of the subsequent discussion is as follows. In Sec. II, we describe the static (undriven) version of the model to recapitulate its symmetries. We also introduce the Floquet formalism and briefly discuss the spectra. In Sec. III, we shall discuss our results on the sinusoidal drive, where the explicit time dependence is eliminated via the Shirley-Floquet approach. Further, we have explored the analytical behavior of the Hamiltonian in the high-frequency regime. Finally, we shall discuss the δ -kick scenario, where easy factorization of the time evolution operator yields a way to analyze various topological invariants. At the end, we summarize and conclude our findings in Sec. IV.

II. THE HAMILTONIAN AND THE FLOQUET FORMALISM

The Creutz ladder consists of two rungs of lattice sites that are coupled by diagonal (t_D), vertical (t_V), and horizontal (t_H) hoppings, as shown in Fig. 1. There are two sublattices a_n , b_n within each unit cell. The real-space Hamiltonian can be written as

$$\begin{aligned}
 H_0 = & - \sum_n t_H (e^{i\theta} a_n^\dagger a_{n+1} + e^{-i\theta} a_{n+1}^\dagger a_n + e^{-i\theta} b_n^\dagger b_{n+1} \\
 & + e^{i\theta} b_{n+1}^\dagger b_n) + t_D (a_n^\dagger b_{n+1} + b_{n+1}^\dagger a_n + a_{n+1}^\dagger b_n \\
 & + b_n^\dagger a_{n+1}) + t_V (a_n^\dagger b_n + b_n^\dagger a_n), \quad (1)
 \end{aligned}$$

$$H_0 = H_H + H_D + H_V. \quad (2)$$

The complex phase, θ , associated with the horizontal hopping leads to a destructive interference, as a consequence of which localization of particles for a certain region of parameter space is observed. The Creutz ladder shows a flat band dispersion for the rungless case ($t_V = 0$), implying that group velocities

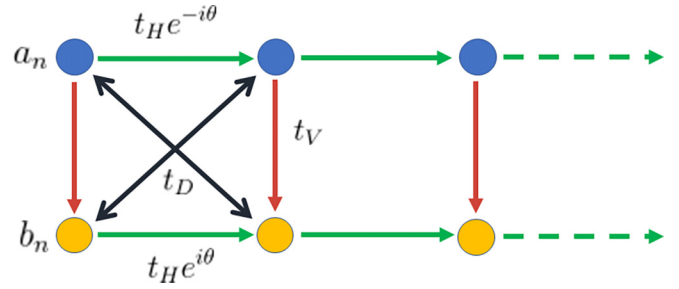


FIG. 1. The figure depicts a schematic representation of the quasi-1D Creutz ladder, where a_n and b_n denote the two distinct sublattices. The different hopping amplitudes t_H , t_V , and t_D denote the horizontal, vertical, and diagonal hoppings, respectively.

of the resulting states are zero. In an open boundary condition, this leads to complete localization of states at the edges.

In momentum space, the Hamiltonian reads as

$$\begin{aligned}
 H_0(k) = & 2t_H \cos(k) \cos(\theta) \sigma_0 + 2t_H \sin(k) \sin(\theta) \sigma_z \\
 & + [t_V + 2t_D \cos(k)] \sigma_x. \quad (3)
 \end{aligned}$$

Here $\sigma_i = x, y, z$ are the Pauli matrices. If ϕ denotes the total flux through each plaquette, then $2\theta = \frac{\phi}{\phi_0}$, where ϕ_0 denotes the magnetic flux quantum.

At this point it is important to talk about the symmetries of the model [39,44,49,50]. The model has an inherent inversion symmetry with respect to an axis that lies symmetrically between the two legs of the ladder. It is expressed by the relation $\sigma_x H_0(k) \sigma_x = H_0(-k)$. Furthermore, it possesses a chiral symmetry that is illustrated by $\sigma_y H_0(k) \sigma_y = -H_0(k)$, only for the values $\theta = \frac{\pi}{2}$. In spite of the presence of a magnetic field, the system has an inherent time-reversal symmetry given by $\sigma_x H_0^*(k) \sigma_x = H_0(-k)$. Lastly, a particle-hole symmetry exists in the system for $\theta = \frac{\pi}{2}$, which can be illustrated by $\sigma_z H_0^*(k) \sigma_z = -H_0(-k)$.

Now we are all set to study the Floquet topological aspects of the periodically driven model, which in a Creutz ladder enters through the modulation of the hopping amplitudes in time. To set the notations, let us start our discussion for a generic Hamiltonian, by considering the driving in the form of a sinusoidal variation, that is, $H(t) = H_0 + 2V_0 \cos \omega t$, with V_0 and ω , being the driving amplitude and the driving frequency, respectively, and H_0 is a generic static Hamiltonian. The properties of interest in our work can be obtained using Floquet theory [51–53], according to which the time-dependent Schrödinger equation can be solved using the Floquet ansatz, $|\psi(t)\rangle = e^{-iEt} |u(t)\rangle$, where $|u(t+T)\rangle = |u(t)\rangle$ denotes the time-periodic Floquet modes, and E represents the Floquet quasienergies. These Floquet states are also the eigenstates of the Floquet evolution operator. We can find E and $|u_k(t)\rangle$ by solving the Floquet-Bloch equation,

$$[H(t) - i\partial_t] |u_k(t)\rangle = E |u_k(t)\rangle. \quad (4)$$

The operator $H(t) - i\partial_t = H_F$ is termed as the Floquet Hamiltonian. Because of the time periodicity, it is convenient to consider the composite Hilbert space $\mathcal{R} \otimes \mathcal{T}$, where \mathcal{R} is the usual Hilbert space with a complete set of orthogonal basis, and \mathcal{T} is the space of time-periodic functions spanned

by $e^{-im\omega t}$. This yields the following form of H_F ,

$$H_F = \sum_{m,m'} \left(m\omega \delta_{m,m'} + \frac{1}{T} \int_0^T dt H(t) e^{-i(m-m')\omega t} \right). \quad (5)$$

This leads to a situation where we can split the driven spectrum into an infinite number of copies of the undriven Hamiltonian separated by $m\omega$; that is, the index m defines a subspace, called the m th Floquet replica. A general representation of the Floquet Hamiltonian thus can be represented as

$$H_F = \begin{bmatrix} \ddots & \vdots & \vdots & \vdots & \vdots & \vdots & \ddots \\ \dots & H_0 - 2\omega & H_{-1} & H_{-2} & H_{-3} & H_{-4} & \dots \\ \dots & H_1 & H_0 - \omega & H_{-1} & H_{-2} & H_{-3} & \dots \\ \dots & H_2 & H_1 & H_0 & H_{-1} & H_{-2} & \dots \\ \dots & H_3 & H_2 & H_1 & H_0 + \omega & H_{-1} & \dots \\ \dots & H_4 & H_3 & H_2 & H_1 & H_0 + 2\omega & \dots \\ \ddots & \vdots & \vdots & \vdots & \vdots & \vdots & \ddots \end{bmatrix}, \quad (6)$$

where the elements $H_{\pm m} = \frac{1}{T} \int_0^T H(t) e^{\pm im\omega t} dt$ get rid of the explicit time dependence.

Coming back to our context of the Creutz ladder, it is important to understand the consequences of adding periodic drives to either one, two, or all three hoppings, namely, t_V , t_D , and t_H . For instance if we include a drive to the horizontal hopping (t_H) then in the Fourier space of H_F , $H_{\pm m}$ will appear in the form of an identity matrix. Physically this suggests that the drive fails to induce overlap of different Floquet replicas, and hence the system cannot generate the so called π energy modes at the boundaries of the Floquet BZ. A clearer picture will emerge from the subsequent discussions. In order to realize meaningful Floquet topological features, we must associate the drive to either the diagonal hopping (t_D) or the vertical hopping (t_V). In both these cases, the drive connects different sublattice degrees of freedom. While we have verified that the scenarios for t_D and t_V are qualitatively similar, we have chosen the Floquet driving in t_V for our numeric computation.

III. RESULTS

A. Sinusoidal drive

We first describe the harmonic drive, associated only with the vertical hopping (t_V), which can be written as

$$H_V(t) = (2V_0 \cos \omega t + t_V) \sum_n (a_n^\dagger b_n + a_n b_n^\dagger). \quad (7)$$

The rest of the terms in Eq. (1) are left unaltered. The Fourier components $|H|_{\pm m}$ except for $m = 0, \pm 1$ vanish owing to the mathematical form of the drive. Hence we can truncate the infinite-dimensional matrix into a 3×3 block and can study the corresponding quasienergy spectrum. By using Floquet theory we can show that driving induces additional gaps and edge states depending upon the driving frequency and the strength of the driving field. Before going into that, we reemphasize that for our purpose the chiral symmetry of the model is of prime importance. Since the emergence of the π energy modes is protected by the chiral symmetry, we fix a particular value of the phase, namely $\theta = \frac{\pi}{2}$. Let us first briefly

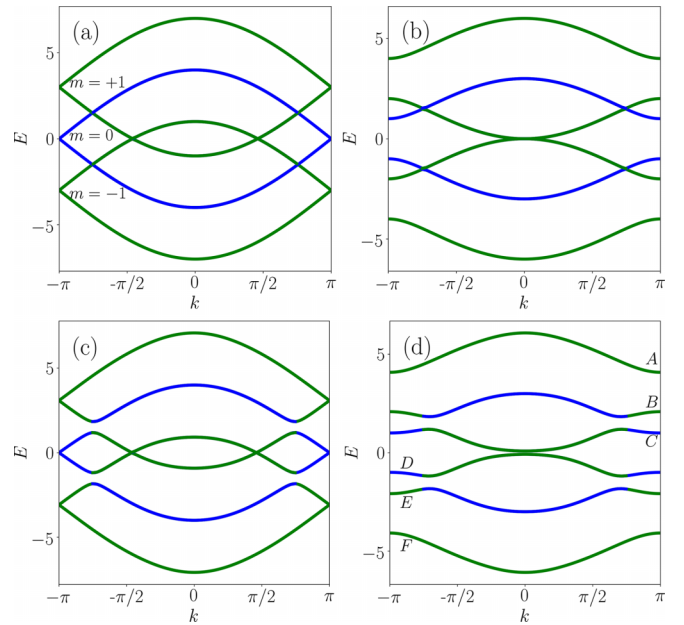


FIG. 2. The Floquet quasienergy spectrum in the frequency space with $m \in [-1, 1]$, obtained for different sets of values of the hopping parameters as well as the driving amplitude, V_0 . The opening and closing of the zero and the π gaps are clearly illustrated. The parameters used are $(t_V, t_D) = (2, 1)$ in panels (a) and (c) and $(t_V, t_D) = (1, 1)$ in panels (b) and (d). The amplitude of the drive is chosen as $V_0 = 0$ for panels (a) and (b), whereas $V_0 = 0.5$ for panels (c) and (d). The rest of the parameters are chosen as $t_H = 1$, $\omega = 3$, $\theta = \pi/2$.

recapitulate the topological properties of the static model. The topological phase transition is signaled by the ratio $\frac{t_V}{2t_D}$. The system shows nontrivial behavior for $\frac{t_V}{2t_D} < 1$ and trivial behavior $\frac{t_V}{2t_D} > 1$. Figures 2(a) and 2(b) show the spectra for $t_V = 2t_D$ and $t_V \neq 2t_D$, respectively. While the former denotes a gap closing scenario, at $k = \pm\pi$ (the lattice constant is taken as unity), the latter does have a gap at the edges of the BZ with a magnitude $\Delta = 2|t_V - 2t_D|$. The color scale represents different replicas; for example, blue denotes $m = 0$, whereas green denotes $m = \pm 1$. The importance of topology can be explored at the points $E = 0, \pm\frac{\pi}{T}$ ($\pm\frac{\pi}{T}$ is equivalent to $\pm\frac{\omega}{2}$), where the spectra show degeneracies.

Once the time-dependent perturbation is switched on as shown in Figs. 2(c) and 2(d) the degeneracies at $\pm\frac{\omega}{2}$ (involving states with $m = 0, m = \pm 1$) are lifted, leading to the formation of drive-induced band gaps, with magnitude $\Delta \approx 4|V_0|$. One can also verify, since the energy spectrum is symmetric about $\pm m\omega/2$, the π gap opening relies on the presence of the chiral symmetry of the system. Even when the frequency is very high, the zero and the π gaps remain open, but different replicas are widely separated from each other. This prohibits any overlap between the $m = 0, m \neq 0$ bands. On the other hand, for low frequencies, more replicas start overlapping, and inside the spectrum of $m = 0$ we observe a large number of degeneracies due to the mixing of different bands.

In order to show evidence of the topological phase transition in our driven scenario, we need to consider the Floquet

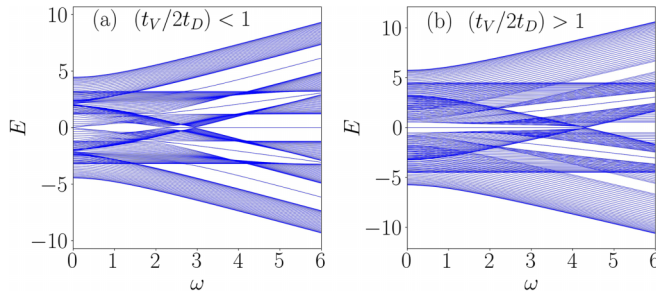


FIG. 3. The Floquet real-space quasienergy spectrum as a function of the driving frequency, ω . Panel (a) corresponds to the static nontrivial condition with the parameter choice $(t_V, t_D) = (1, 1)$. Panel (b) corresponds to the static trivial condition with the parameter choice $(t_V, t_D) = (2.2, 1)$. The remaining parameters are chosen as $t_H = 1$, $\theta = \pi/2$, $V_0 = 0.5$.

spectrum of a semi-infinite system in a wide range of frequencies. Due to the existence of an edge, one can infer the topological character from the presence of edge states. Figure 3 shows the driven quasienergy spectrum in both the situations that correspond to trivial ($\frac{t_V}{2t_D} > 1$) and topological ($\frac{t_V}{2t_D} < 1$) pertaining to the static case. In the subsequent discussions, the parameters such as E , t_V , t_D , ω , V_0 are measured in units of t_H , where we have set $t_H = 1$. As soon as the time-dependent perturbation is switched on, the π energy modes appear, which have an extended nature up to a certain range of frequencies depending upon the magnitude of the band gap between $E = \pm \frac{\omega}{2}$ states. However in the limit $\frac{t_V}{2t_D} > 1$, for which the system was completely trivial, now in the presence of driving it shows nontrivial behavior with the emergence of zero energy modes [see Fig. 3(b)]. One can also verify, for the rungless case ($t_V = 0$), due to flat-band-like dispersion, there is no possible overlapping between different replicas, and hence, we cannot generate localized π energy modes even when the drive is intact ($V_0 \neq 0$).

If one can interpret the hopping parameters as $t_V = t_0 + \delta$ and $2t_D = t_0 - \delta$, then analytically we can set a threshold value of the frequency, say $\omega = 2t_0$. Above this value, in the static topological limit ($\frac{t_V}{2t_D} < 1$), the system hosts the zero energy mode, whereas in the static trivial limit ($\frac{t_V}{2t_D} > 1$) the system preserves its zero energy mode up to this threshold frequency. For example in Fig. 3(a), for the parametric choice $(t_V, t_D) = (1, 1)$, the zero energy mode is formed at a frequency, ω such that $\omega > 2t_0$ [$\omega = 3$ in Fig. 3(a)], whereas in Fig. 3(b) for the parametric choice $(t_V, t_D) = (2.2, 1.0)$, the zero energy mode is preserved up to a frequency ω , such that $\omega < 2t_0$ [$\omega = 4.2$ in Fig. 3(b)]. Hence, we say for frequency $\omega > 2t_0$, close to $E = 0$, the topology of the driven system corresponds to that of the undriven one. We label this regime as the high-frequency regime. Similarly close to $E = \pm \frac{\omega}{2}$, the high-frequency regime corresponds to $\omega > 4t_0$, where the spectral gaps at $E = \pm \frac{\omega}{2}$ are nonexistent. One can also notice that in the static nontrivial limit ($\frac{t_V}{2t_D} < 1$), there are no zero energy modes up to $\omega = 2t_0$. This can alternatively be verified from the bulk spectrum, where within the frequency range $\omega < 2t_0$, although the spectral gaps at the edges of the BZ are open, there are other gapless points

corresponding to the $m = 0$ replica. As we increase more branches, for example $m = \pm 1$ (or even $m = \pm 2$, etc.), spectral gaps open up at these degenerate points. However, these are π energy modes, and we have no zero energy modes for $\omega < 2t_0$. Based on the above discussions, we may conclude that under static nontrivial conditions ($\frac{t_V}{2t_D} < 1$), the driven system has no zero energy mode in the low-frequency regime, whereas, under static trivial condition ($\frac{t_V}{2t_D} > 1$), the driven system has no zero energy mode in the high-frequency regime.

To further confirm the topological signatures in terms of “bulk-edge correspondence,” we resort to the calculation of the topological invariant [54]. The relevant invariant for a 3×3 Floquet-Bloch Hamiltonian in the frequency domain is the Berry phase [55,56], which denotes the geometric phase acquired by a wave function as the system is smoothly taken across the Brillouin zone. A Hamiltonian with a nontrivial Berry phase cannot be adiabatically connected to an atomic insulator unless a gap closing transition occurs. The Berry phase is defined as

$$\gamma = i \oint dk \langle u_k | \nabla_k u_k \rangle, \quad (8)$$

where $|u_k\rangle$ are the Bloch states. The numerical calculation of the Berry phases γ_α [α denotes band index, marked with the letters A–F in Fig. 2(d)] for each of the bands for a particular frequency, say, $\omega = 4.5$, in units of t_H , is obtained as

$$\gamma_\alpha = \begin{cases} 0, & (\alpha = A, F), \\ \pi, & (\alpha = B, C, D, E), \end{cases} \quad \text{for } \left(\frac{t_V}{2t_D}\right) > 1, \quad (9)$$

$$\gamma_\alpha = \begin{cases} \pi, & (\alpha = A, F), \\ 0, & (\alpha = B, C, D, E), \end{cases} \quad \text{for } \left(\frac{t_V}{2t_D}\right) < 1. \quad (10)$$

It is interesting to note that there is at least one band below the Fermi level that corresponds to the nonzero Berry phase, and thus signals that the system is in a topologically nontrivial state. Hence, irrespective of the choice of whether $t_V > 2t_D$ or otherwise, the topological properties of a driven Hamiltonian are now controlled by frequency of the driving field. One can also verify that the cumulative sum of Berry phases, that is, $\gamma = |\text{mod}(\sum_\alpha \gamma_\alpha, 2)|$, corresponds to the edge states found in the real-space spectrum. Figures 4(a) and 4(b) and Figs. 4(c) and 4(d) show the results for the cumulative sum of the Berry phase up to $E = 0$ (zero mode) and $E = \frac{\pi}{7}$ (π mode) corresponding to the nontrivial and trivial limits for the undriven case.

B. Floquet-Magnus effective Hamiltonian

To analyze the correct analytical behavior of the Floquet Hamiltonian for large frequencies, that is, $\omega > 2t_0$, we resort to the high-frequency calculation, which involves a rotating frame transformation in the Floquet formalism. In the rotating frame, given by unitary transformation $S(t)$, the transformed Floquet Hamiltonian Eq. (6) takes the form

$$\begin{aligned} \tilde{H}_k(t) &= S^\dagger(t) H_F(t) S(t) \\ &= S^\dagger(t) H_k(t) S(t) - i S^\dagger(t) \dot{S}(t). \end{aligned} \quad (11)$$

We may choose to work with some particular choices for rotating frames, where the unitary transformation is

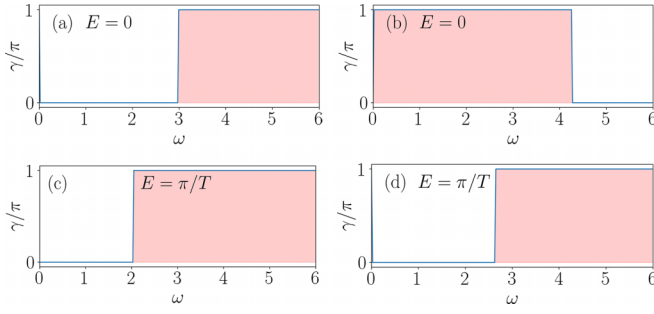


FIG. 4. The panels depict total Berry phases for the states filled up to $E = 0$ and π/T , as a function of the driving frequency, ω . Panels (a) and (c) give the total Berry phases for the zero and the π energy modes, respectively, under static nontrivial conditions, with the parameter choice being $(t_V, t_D) = (1, 1)$. Panels (b) and (d) give the total Berry phases for the zero and the π energy modes, respectively, under static trivial conditions, with the parameter choice being $(t_V, t_D) = (2.2, 1)$. Other parameters are chosen as $t_H = 1$, $\theta = \pi/2$, $V_0 = 0.5$.

defined as

$$S(t) = e^{i\theta(t)\sigma_x}, \quad \theta(t) = \frac{\alpha\omega t}{2} + \frac{2V_0 \sin \omega t}{\omega}, \quad (12)$$

so that the transformed Hamiltonian $\tilde{H}_k^\alpha(t)$ can be written as

$$\begin{aligned} \tilde{H}_k^\alpha(t) = & 2t_H(\sin k)e^{2i\theta\sigma^+} + 2t_H(\sin k)e^{-2i\theta\sigma^-} \\ & + \left(t_V - \frac{\alpha\omega}{2} + 2t_D \cos k\right)\sigma_x, \end{aligned} \quad (13)$$

where

$$\sigma^\pm = \frac{\sigma_z \pm i\sigma_y}{2}. \quad (14)$$

Note that the modified Hamiltonian $[\tilde{H}_k^\alpha(t)]$ shares the same periodicity as that of the original one $[H(t)]$. With $\tilde{H}_k^\alpha(t)$ being periodic in time, the Fourier decomposition, $\tilde{H}_k^\alpha(t) = \sum_p e^{ip\omega t} \tilde{H}_{p,k}^\alpha$, with $p = 0, \pm 1, \pm 2, \dots$ and so on, allows us to write an expansion in powers of the inverse of the driving frequency, namely, $1/\omega$, which is known as the Magnus expansion [57–59]. This yields an effective Hamiltonian H_{eff} , given by

$$\begin{aligned} H_{\text{eff}} = & \tilde{H}_{0,k}^\alpha + \frac{1}{\omega} [\tilde{H}_{0,k}^\alpha, \tilde{H}_{1,k}^\alpha] - \frac{1}{\omega} [\tilde{H}_{0,k}^\alpha, \tilde{H}_{-1,k}^\alpha] \\ & - \frac{1}{\omega} [\tilde{H}_{-1,k}^\alpha, \tilde{H}_{1,k}^\alpha] + O\left(\frac{1}{\omega^2}\right), \end{aligned} \quad (15)$$

where, $[\tilde{H}_{p,k}^\alpha, \tilde{H}_{p',k}^\alpha]$ denotes a commutator. The convergence criterion of the expansion is given by

$$\int_0^T \|\tilde{H}_k^\alpha(t) dt\| < \pi. \quad (16)$$

There is a subtle point about the choices of the reference frames that deserves a mention. The Hamiltonian $\tilde{H}_k^\alpha(t)$ in different time frames has different convergence criteria, that should depend upon values of α . For example, in the high-frequency regime, that is, $\omega > 2t_0$, the convergence criterion is satisfied by the choice $\alpha = 0$, whereas for any intermediate frequency range, say, $t_0 < \omega < 2t_0$, the series converges for

$\alpha = 1$, provided $\frac{t_V}{2t_D} > 1$. However, for $\omega < t_0$, the approximation starts failing. By using the expansion [60,61]

$$e^{iz \sin \theta} = \sum_{n=-\infty}^{\infty} \mathcal{J}_n(z) e^{in\theta}, \quad (17)$$

with \mathcal{J}_n being the n th-order Bessel function of the first kind, the Fourier component of the transformed Hamiltonian can be written as

$$\begin{aligned} \tilde{H}_{p,k}^\alpha = & \left(t_V - \frac{\alpha\omega}{2} + 2t_D \cos k\right)\sigma_x \\ & + \left[2t_H \sin k \mathcal{J}_{p-\alpha}\left(\frac{2V_0}{\omega}\right)\right]\sigma^+ \\ & + \left[2t_H \sin k \mathcal{J}_{p-\alpha}\left(\frac{2V_0}{\omega}\right)\right]\sigma^-. \end{aligned} \quad (18)$$

Within the region of convergence, $\tilde{H}_{0,k}^\alpha$ is the dominant term, whereas the other components can be neglected owing to the fact that the Bessel functions \mathcal{J}_p decay rapidly for $p \neq 0$. Hence, the time-independent effective Hamiltonian can be written as

$$H_{\text{eff}} = (t_V^{\text{eff}} + 2t_D \cos k)\sigma_x + 2t_H^{\text{eff}} \sin k \sigma_z, \quad (19)$$

where

$$t_H^{\text{eff}} = t_H \mathcal{J}_{-\alpha}\left(\frac{2V_0}{\omega}\right), \quad t_V^{\text{eff}} = t_V - \frac{\alpha\omega}{2}. \quad (20)$$

The effective Hamiltonian in the momentum space can be expressed as a massless Dirac equation of the form

$$H(k) = \vec{d}(k) \cdot \vec{\sigma}, \quad (21)$$

where $\vec{\sigma}$ denotes the Pauli matrices ($\sigma_x, \sigma_y, \sigma_z$) and $d(k)$ s are the corresponding vector components, having the forms

$$d_x(k) = t_V - \frac{\alpha\omega}{2} + 2t_D \cos k, \quad (22a)$$

$$d_z(k) = t_H \mathcal{J}_{-\alpha}\left(\frac{2V_0}{\omega}\right) \sin k. \quad (22b)$$

Hence, the topological properties of the system can be quantified by the invariant called the winding number, defined as [54,62]

$$\nu = \frac{1}{2\pi} \int_0^{2\pi} \frac{d_z d(d_x) - d_x d(d_z)}{d_x^2 + d_z^2} dk. \quad (23)$$

Mathematically, the winding number quantifies how many times the vector $\vec{d}(k)$ winds around the origin as k is varied over the BZ. Physically, the winding number carries the same information as the Berry phase which we have already obtained earlier.

In Fig. 5, we have plotted the topological phase diagram in terms of the winding number, for two cases, say, for $\omega > 2t_0$ [Fig. 5(a)] and for $\omega = 1.2t_0$ [Fig. 5(b)]. We see a sharp change in the value of the winding number from $\nu = 0$ to a finite value of ν . Additionally, in the nontrivial region, a new topological phase, characterized by $\nu = -1$, appears. The transition between different topological phases, corresponding to $\nu = 1$ and $\nu = -1$, occurs at zeros of the Bessel function, $\mathcal{J}_{-\alpha}\left(\frac{2V_0}{\omega}\right)$. Hence, the different topological phases are characterized by the winding number, $\nu = \text{sgn} \mathcal{J}_{-\alpha}\left(\frac{2V_0}{\omega}\right)$.

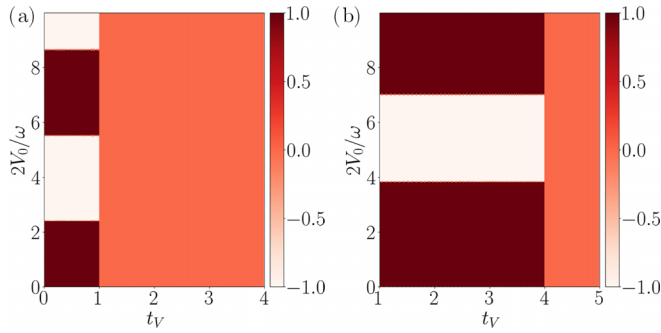


FIG. 5. The topological phase diagram of Floquet-Magnus effective Hamiltonian. Panel (a) corresponds to $\omega > 2t_0$ and panel (b) corresponds to $\omega = 1.2t_0$. The topological-trivial phase transition occurs at $t_V = 1$ in panel (a) and $t_V = 4$ in panel (b). The parameters are chosen as $t_D = 0.5$, $\theta = \pi/2$.

Further, we can compare the quasienergy spectra as well as the topological phase diagrams corresponding to both H_F and H_{eff} . When a truncation to high enough ω is applied to H_F , its spectrum should be close enough to the exact Floquet effective Hamiltonian obtained from the time-ordered product of the Floquet evolution operator. Further, for a fixed value of ω , the quasienergy spectrum of H_F can be confined to the first quasienergy BZ $[\pi/T : \pi/T]$ or $[-\omega/2 : \omega/2]$ [see Fig. 6(a)]. Depending upon different convergence criteria at different ranges of frequencies, we have shown the quasienergy spectrum corresponding to H_{eff} only in the region $\omega > t_0$, which further can be split into two cases, such that $\omega > 2t_0$ [see Fig. 6(b)] and $t_0 < \omega < 2t_0$ [see Fig. 6(c), which is plotted for $\omega = 1.2t_0$].

Let us start by comparing the outcomes of two methods by fixing the parameters as $t_D = 0.5$, $V_0 = 0.5$, $\omega = 3$. For $\omega > 2t_0$, the results obtained by both the methods show features similar to that of a static one, where the system is nontrivial (trivial) for $t_V < 1$ ($t_V > 1$), whereas for the other, namely, $t_0 < \omega < 2t_0$, we observe longer-range hoppings induced by the periodic driving. As a result, one can get topologically protected zero energy modes even when t_V is very large.

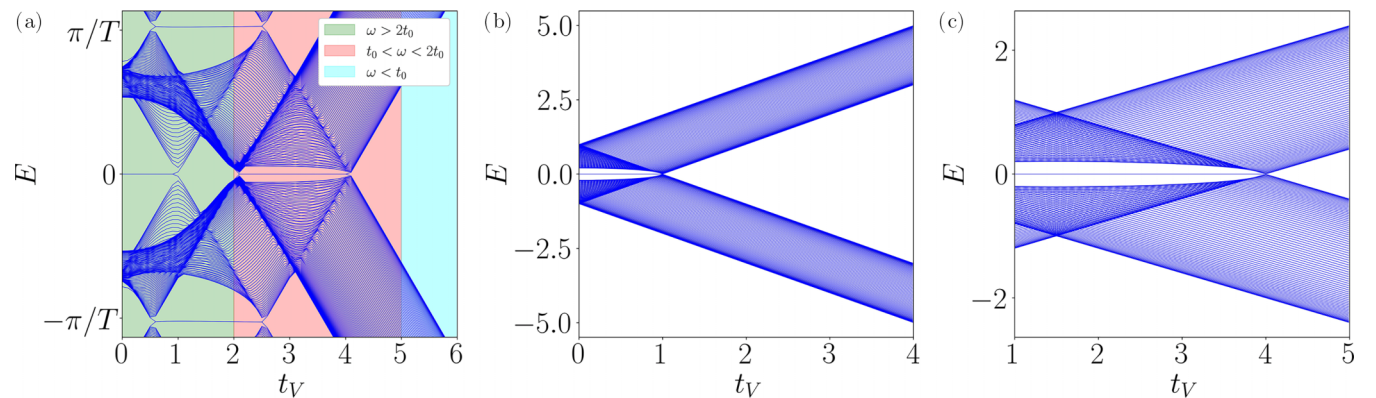


FIG. 6. Panel (a) shows the Floquet quasienergy spectrum [obtained by the direct truncation of the Hamiltonian in Eq. (6), namely, H_F] inside the first FBZ, as a function of the vertical hopping parameter (t_V), whereas panels (b) and (c) show the quasienergy spectrum corresponding to the Floquet-Magnus effective Hamiltonian for $\omega > 2t_0$ and in the range $t_0 < \omega < 2t_0$ (for concreteness we have taken $\omega = 1.2t_0$), respectively. In panel (a) different frequency regimes are shown via different colors indicated in the figure. The other parameters are chosen as $\omega = 3$ [in panel (a)], $t_D = 0.5$, $V_0 = 0.5$, $t_H = 1$.

However, it is clear from the figures that in the region $t_0 < \omega < 2t_0$, the spectra of H_F and H_{eff} show significantly different features. For example, in the case of the Magnus effective Hamiltonian (H_{eff}), topologically protected zero energy modes will always emerge at $\frac{t_V}{2t_D} > 1$ or $t_V > 1$, and it will continue to exist up to a certain value of t_V , depending upon the value of frequency under consideration, inside the region $t_0 < \omega < 2t_0$. However, this is not true for the truncated Hamiltonian, H_F , where the region $t_0 < \omega < 2t_0$ comes into existence for $t_V > 2$. Again the range of the zero energy modes will be dependent upon the frequencies we are working with. Furthermore, we have seen that for $\omega < t_0$, due to the breakdown in the convergence criteria, the Floquet Magnus effective Hamiltonian (H_{eff}) fails to yield correct topological properties. This is supported by the quasienergy spectrum obtained using H_F [see Fig. 6(a)], which does not show any evidence of the localized zero energy modes in the region $\omega < t_0$.

We can also compare the corresponding topological phase diagrams obtained via the two Hamiltonians, namely, H_F and H_{eff} . It should be noted that the topological phase diagram corresponding to the truncated Floquet Hamiltonian, H_F , is enumerated via the Berry phase, whereas for the Magnus approximated Hamiltonian the winding number is used [Figs. 5(a) and 5(b)]. It can also be shown that the phase diagrams based on the winding number for the time-ordered Floquet evolution operator show identical results to that of the Berry phase corresponding to H_F . The computation of the winding number in this case relies on the mechanism of symmetric time frames, which we shall explain in the next section. From the study of the topological phase diagram, it has been clear that for $\omega > 2t_0$, both the methods show features similar to the static one, whereas in the limit $t_0 < \omega < 2t_0$, there are some regions where the spectra corresponding to H_F and H_{eff} are significantly different. Hence, in the limit $t_0 < \omega < 2t_0$, using H_{eff} to study the topological phase diagram could be problematic, while H_F is expected to yield identical results to that of the time-ordered product Hamiltonian. Moreover, for $t_0 < \omega < 2t_0$, due to the failure of the convergence criterion laid down in Eq. (16), the winding number becomes ill defined in the region where $\frac{t_V}{2t_D} < 1$. This is supported by

the quasienergy spectrum obtained using H_F , which does not show any evidence of localized zero energy modes in the region $\frac{t_V}{2t_D} < 1$ for $\omega < 2t_0$.

C. δ kick

In this section we will discuss another variant of periodic drive, namely, a δ kick, again associated with the vertical hopping (t_V) such that the Hamiltonian becomes

$$H_V(t) = \left[t_V + V_0 \sum_{m=-\infty}^{m=\infty} \delta(t - mT) \right] \sum_n (a_n^\dagger b_n + a_n b_n^\dagger). \quad (24)$$

Unlike the sinusoidal case, the Floquet Hamiltonian corresponding to such a kick cannot be expanded in the frequency domain [see Eq. (6)], since the truncation of the infinite-dimensional matrix is not possible. Rather, a different technique is followed here. We consider the Floquet time evolution operator defined as

$$U(T) = \mathcal{T} e^{-i \int_0^T dt H(t)}, \quad (25)$$

where \mathcal{T} is the time-ordering operator. Now using the Suzuki-Trotter decomposition of the first kind [63], for a δ -driven Hamiltonian, the Floquet time evolution operator can be written as a product of two exponential matrices, which are

$$U(T) = e^{-iV_0 \sum_n (a_n^\dagger b_n + a_n b_n^\dagger)} e^{-iH_0 T} = e^{-iH_{\text{eff}} T}, \quad (26)$$

where H_{eff} is the time-independent effective Hamiltonian analogous to H_F [Eq. (6)] that we had obtained corresponding to the sinusoidal case. Now to study the Floquet quasienergy spectrum, we plot the eigenvalues of H_{eff} which will be confined within the FBZ, namely, $(-\frac{\pi}{T} : \frac{\pi}{T})$ shown in Fig. 8(a). Similarly in the momentum space Eq. (26) can be written as

$$U_k(T) = e^{-iV_0 \sigma_x} e^{-iH_0(k)T} = e^{-iH_{\text{eff}}(k)T}. \quad (27)$$

Here, the topological invariant is again the winding number. The effective Hamiltonian obtained in this way has the form of a massless Dirac equation with all three components of the $\vec{d}(k)$ vector being present. The components of the d vectors in this case are

$$d_x(k) = - \frac{E_k}{\sin(E_k T)} \left[\sin V_0 \cos(E_{k,0} T) + \frac{t_V + 2t_D \cos k}{E_{k,0}} \cos V_0 \sin(E_{k,0} T) \right], \quad (28)$$

$$d_y(k) = \frac{E_k}{\sin(E_k T)} \left[\frac{t_H \sin k}{E_{k,0}} \sin V_0 \sin(E_{k,0} T) \right], \quad (29)$$

$$d_z(k) = - \frac{E_k}{\sin(E_k T)} \left[\frac{t_H \sin k}{E_{k,0}} \cos V_0 \sin(E_{k,0} T) \right], \quad (30)$$

where $E_{k,0}$ is the eigenvalue of the undriven model, and E_k is the quasienergy of the effective Hamiltonian,

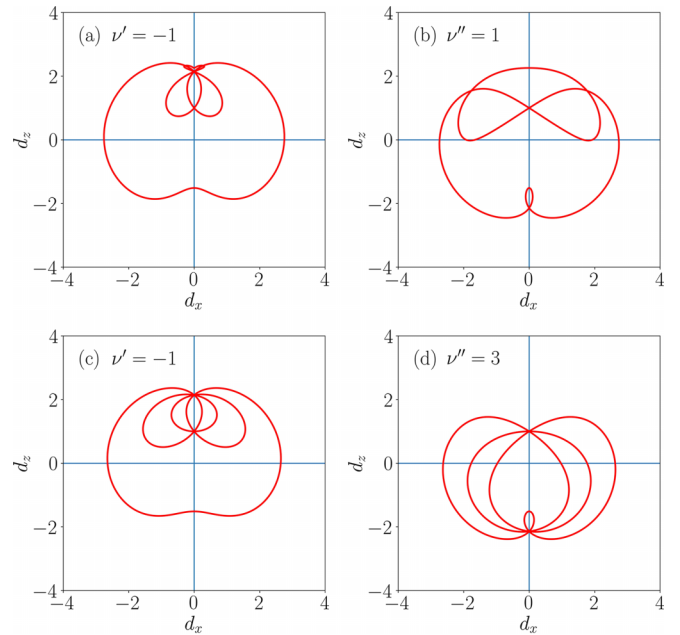


FIG. 7. The closed curves in the d_x - d_z plane for both chiral symmetric time frames with winding number being ν' and ν'' , respectively. The parameters used are $(t_V, t_D) = (1.0, 1.5)$ in panels (a) and (b) and $(t_V, t_D) = (2.0, 1.0)$ in panels (c) and (d). The other parameters are chosen as $t_H = 1$, $V_0 = 0.5$, $\theta = \pi/2$, $\omega = 2.5$.

given by

$$E_k = \frac{1}{T} \arccos \left[\cos V_0 \cos(E_{k,0} T) - \frac{t_V + 2t_D \cos k}{E_{k,0}} \sin V_0 \sin(E_{k,0} T) \right]. \quad (31)$$

Apparently the chiral symmetry of H_{eff} loses its meaning. Since, unlike the static version of the Creutz ladder, due to the presence of σ_y in the Bloch Hamiltonian, H_{eff} , here the parameter vector $\vec{d}(k)$ does not lie on the x - z plane. Consequently, the winding about any arbitrary axis becomes difficult to visualize. As a remedy, we rely on the mechanism of a pair of “symmetric time frames,” which are defined by the choice of time frames, resulting in the Floquet evolution operator assuming a form

$$\hat{U} = \hat{F} \hat{G}, \quad (32)$$

where \hat{F} and \hat{G} are related by the chiral symmetry operator as

$$\hat{C} \hat{F} \hat{C} = \hat{G}^{-1}. \quad (33)$$

It is also easy to verify that if a symmetric time frame exists corresponding to a Floquet evolution operator $\hat{U}' = \hat{F} \hat{G}$, then also there must exist another symmetric time frame corresponding to the Floquet operator $\hat{U}'' = \hat{G} \hat{F}$. However, the geometrical picture of winding in either of the frames does not necessarily give complete information about the number of edge modes (generalization of this cannot be done for any arbitrary system). Rather, based on the periodic table of FTIs [64] each of the nontrivial phases of the system can be characterized by a pair of winding numbers ν^0 and ν^π ,

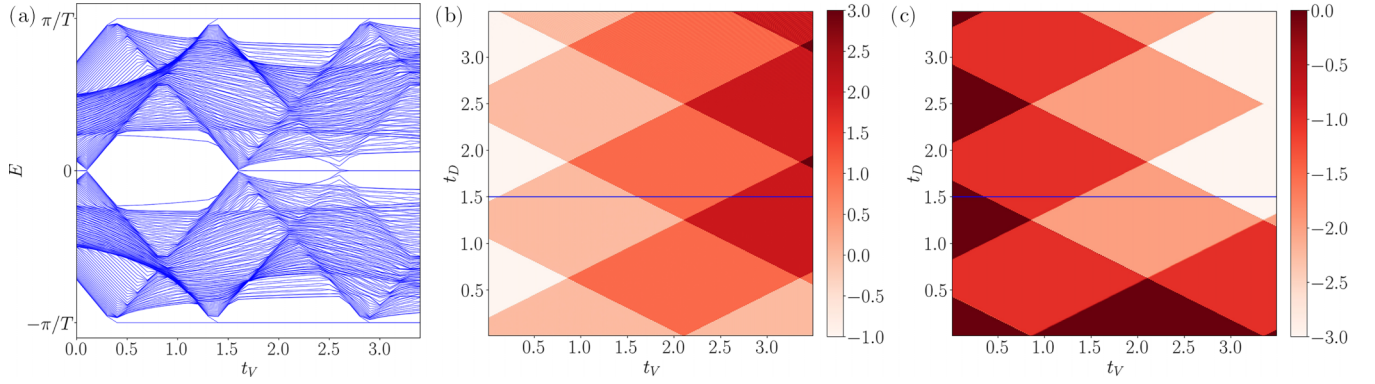


FIG. 8. Panel (a) shows the Floquet quasienergy spectrum inside the first FBZ, as a function of the vertical hopping parameter (t_V) and with fixed diagonal hopping ($t_D = 1.5$) for the δ -kick case. The topological phase transitions are marked by the gap closing at $E = 0$ and π/T with the corresponding appearance or disappearance of the zero and π energy modes. Panels (b) and (c) depict the topological phase diagram in the t_V - t_D plane, computed using the winding numbers corresponding to the zero (ν^0) and the π (ν^π) energy modes, respectively. The parameters used are $\omega = 2.5$, $V_0 = 0.5$, $t_H = 1$.

given by [65–67]

$$\nu^0 = \frac{\nu' + \nu''}{2}, \quad \nu^\pi = \frac{\nu' - \nu''}{2}, \quad (34)$$

where $(\nu^0, \nu^\pi) \in \mathbb{Z} \times \mathbb{Z}$. Further, ν' and ν'' are the winding numbers for the two effective Hamiltonians corresponding to the two symmetric time frames \hat{U}' and \hat{U}'' , respectively. In our model, the Floquet operator in one of the symmetric time frames from $t = T/2$ to $t = 3T/2$ reads as

$$\begin{aligned} U'_k &= e^{-iH_0(k)T/2} e^{-iV_0\sigma_x} e^{-iH_0(k)T/2} \\ &= e^{-iH'_{\text{eff}}(k)T}, \end{aligned} \quad (35)$$

where

$$H'_{\text{eff}}(k) = d'_x(k) \cdot \sigma_x + d'_z(k) \cdot \sigma_z. \quad (36)$$

Similarly, using the chiral symmetry operator, the Floquet time evolution in the second time symmetric frame assumes the form

$$\begin{aligned} U''_k &= e^{-iV_0\sigma_x/2} e^{-iH_0(k)T} e^{-iV_0\sigma_x/2} \\ &= e^{-iH''_{\text{eff}}(k)T}, \end{aligned} \quad (37)$$

where

$$H''_{\text{eff}}(k) = d''_x(k) \cdot \sigma_x + d''_z(k) \cdot \sigma_z. \quad (38)$$

The plots in Fig. 7 show the geometrical picture of winding corresponding to the two chiral symmetric time frames. Finally, when combined, followed by Eq. (34), they can ensure the correct number of zero and π energy modes. Figures 8(b) and 8(c) show the topological phase diagrams in the t_V - t_D plane, plotted for certain values of ω and V_0 given by $\omega = 2.5$ and $V_0 = 0.5$. The confirmation of the bulk-edge correspondence is done by comparing the results with the real-space quasienergy spectrum as a function of t_V plotted for a fixed value of t_D , say, $t_D = 1.5$ [see Fig. 8(a)].

However, a simplified technique to compute the winding numbers following Ref. [68] exists. According to that, the two topological invariants can be found from the half evolution

operator,

$$\hat{U}'_k\left(\frac{T}{2}\right) = \hat{F} = \begin{bmatrix} P_k^\dagger & Q_k \\ -Q_k^\dagger & P_k \end{bmatrix}, \quad (39)$$

in the first symmetric frame as

$$\nu^0 = \nu[Q_k], \quad \nu^\pi = \nu[P_k], \quad (40)$$

where

$$\nu[h] = \frac{1}{2\pi i} \int_{\text{BZ}} dk \frac{d}{dk} \ln h(k). \quad (41)$$

In the static case ($V_0 = 0$), P_k is constant and $Q_k \propto |\vec{d}(k)|$. Thus one finds $\nu^\pi = 0$ and $\nu^0 = \nu$, which is expected. The results obtained by this method are similar to the topological phase diagram already obtained in Fig. 8.

It may be noted that there are regions in the quasienergy spectrum corresponding to certain values of the parameters where the zero and the π energy modes coexist. On the basis of recent studies [17,18], it has been proven that the superposition of the zero and the π energy modes leads to new kinds of symmetry-protected discrete time crystal phases, known as the “period- $2T$ topological Floquet time crystals.” The robustness of this period-doubling feature against any kind of perturbation is supported by computing the two distinct nontrivial gap invariants. As a result, it can be viewed as Rabi oscillations occurring between the two Floquet eigenstates that are split by an amount π/T .

One can also observe that there are instances of gap closing not associated with the topological phase transition (as is well known for the static case) but corresponding to higher values of the winding number. We can verify that as the value of the winding number increases, more states from the bulk become localized states and appear at the edges.

Further, we have studied the variation of the winding numbers (ν^0, ν^π) with respect to the strength of the drive (V_0). Figure 9(a) shows the periodic pattern of the winding numbers, oscillating between zero and finite values. Next, if we fix the strength of the drive, and compute the winding numbers as a function of the time period T [Fig. 9(b)], we observe a linear growth of the winding numbers. However, the steplike

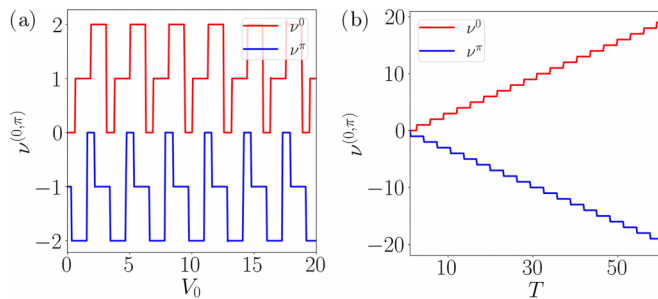


FIG. 9. Panel (a) shows the variation of the winding numbers ($\nu^{(0,\pi)}$) with respect to the strength of the drive (V_0), whereas panel (b) shows the variation of the winding numbers ($\nu^{(0,\pi)}$) with respect to the time period (T). The parameters are chosen as $t_V = t_D = 1.0$, $\omega = 2.5$ in panel (a), whereas $t_V = 2t_D = 1$, $V_0 = 0.5$ in panel (b).

increment can only be obtained corresponding to $t_V = 2t_D$. The results are reminiscent of the plateaus in the Hall resistivity, as seen in quantum Hall effect. The linear growth of the winding numbers can alternatively be understood by the fact that the Baker-Campbell-Hausdorff formula for the computation of the effective Hamiltonian involves a series of commutators that are attached to increasing powers of T . Thus, a large time period can induce progressively longer-range interactions in H_{eff} . As a result, one gets larger values of the winding numbers.

Although our system demonstrates higher values of the winding numbers as a function of T , one should note that as T increases, the existence of robust zero energy modes will suffer owing to the reduced bulk gap in the FBZ $[-\pi/T : \pi/T]$.

IV. FINAL REMARKS

For the undriven Creutz ladder, the topological and the trivial limits are set by $\frac{t_V}{2t_D} < 1$ and $\frac{t_V}{2t_D} > 1$, respectively.

We have taken these values as benchmarks and explored the scenario in a driven system. For the sinusoidal drive, we get at least one band to retain its topological character in the trivial limit ($\frac{t_V}{2t_D} > 1$) as seen from the nonzero Berry phase. Further, the situation nicely distinguishes between the low and the high frequency regimes of the driving potential. Corresponding to the trivial (topological) case, the zero energy mode ceases to exist above (below) a certain value of the driving frequency. The high frequency limit understandably reproduces the results for the static case, which we have explicitly verified using Floquet-Magnus expansion. On the other hand, in the presence of the δ kick, the Creutz ladder presents larger values of the topological invariant, and as a consequence of that, we have a large number of edge modes in the system. Further, the variations of the winding numbers with regard to the time period of the driving, T , yield steplike growth, reminiscent of the quantized Hall plateaus.

It is important to deliberate whether we can define the winding number as the topological invariant for the sinusoidal drive. The answer is affirmative. But unlike the case of the periodic δ kick, the Floquet operator can no longer be expressed as a product of just two operators. Rather, it has to be computed by dividing the time period T into a large number of time steps, each of width Δt , where $\Delta t = \frac{T}{N}$ and N denotes the number of time steps. Hence, one can multiply each of the operators in a time-ordered fashion. The corresponding numerical computation consumes much more time, although it can be done. Indeed the corresponding results are verified by us, and are in excellent agreement with those already obtained from the analysis of the Berry phase.

Note added. Recently, we became aware of Refs. [69,70], where spinful and non-Hermitian Creutz ladders are studied.

-
- [1] C.-R. Yi, L. Zhang, L. Zhang, R.-H. Jiao, X.-C. Cheng, Z.-Y. Wang, X.-T. Xu, W. Sun, X.-J. Liu, S. Chen, and J.-W. Pan, *Phys. Rev. Lett.* **123**, 190603 (2019).
- [2] N. R. Cooper, J. Dalibard, and I. B. Spielman, *Rev. Mod. Phys.* **91**, 015005 (2019).
- [3] D. Hügél and B. Paredes, *Phys. Rev. A* **89**, 023619 (2014).
- [4] L. Jin, *Phys. Rev. A* **96**, 032103 (2017).
- [5] L. Jin and Z. Song, *Phys. Rev. B* **99**, 081103(R) (2019).
- [6] M. Creutz, *Phys. Rev. Lett.* **83**, 2636 (1999).
- [7] S. Gholizadeh, M. Yahyavi, and B. Hetényi, *Europhys. Lett.* **122**, 27001 (2018).
- [8] A. Mukherjee, A. Nandy, S. Sil, and A. Chakrabarti, *Phys. Rev. B* **105**, 035428 (2022).
- [9] J. Cayssol, B. Dóra, F. Simon, and R. Moessner, *Phys. Status Solidi RRL* **7**, 101 (2013).
- [10] M. S. Rudner, N. H. Lindner, E. Berg, and M. Levin, *Phys. Rev. X* **3**, 031005 (2013).
- [11] A. Gómez-León and G. Platero, *Phys. Rev. Lett.* **110**, 200403 (2013).
- [12] M. S. Rudner and N. H. Lindner, *Nat. Rev. Phys.* **2**, 229 (2020).
- [13] A. Agrawal and J. N. Bandyopadhyay, *J. Phys.: Condens. Matter* **34**, 305401 (2022).
- [14] C.-F. Li, L.-N. Luan, and L.-C. Wang, *Int. J. Theor. Phys.* **59**, 2852 (2020).
- [15] K. Yang, S. Xu, L. Zhou, Z. Zhao, T. Xie, Z. Ding, W. Ma, J. Gong, F. Shi, and J. Du, *Phys. Rev. B* **106**, 184106 (2022).
- [16] T.-S. Xiong, J. Gong, and J.-H. An, *Phys. Rev. B* **93**, 184306 (2016).
- [17] Y. Pan and B. Wang, *Phys. Rev. Res.* **2**, 043239 (2020).
- [18] B. Wang, J. Quan, J. Han, X. Shen, H. Wu, and Y. Pan, *Laser Photonics Rev.* **16**, 2100469 (2022).
- [19] D. J. Yates and A. Mitra, *Phys. Rev. B* **96**, 115108 (2017).
- [20] L. Zhou, *Phys. Rev. Res.* **4**, 043164 (2022).
- [21] S. Mondal, D. Sen, and A. Dutta, *J. Phys.: Condens. Matter* **35**, 085601 (2023).
- [22] A. K. Ghosh, T. Nag, and A. Saha, *Phys. Rev. B* **103**, 045424 (2021).
- [23] R. Seshadri, A. Dutta, and D. Sen, *Phys. Rev. B* **100**, 115403 (2019).
- [24] K. Plekhanov, M. Thakurathi, D. Loss, and J. Klinovaja, *Phys. Rev. Res.* **1**, 032013(R) (2019).
- [25] R. W. Bomantara, L. Zhou, J. Pan, and J. Gong, *Phys. Rev. B* **99**, 045441 (2019).

- [26] S. Afzal, T. J. Zimmerling, Y. Ren, D. Perron, and V. Van, *Phys. Rev. Lett.* **124**, 253601 (2020).
- [27] Y. Wang, H. Steinberg, P. Jarillo-Herrero, and N. Gedik, *Science* **342**, 453 (2013).
- [28] W. Lee, Y. Lin, L.-S. Lu, W.-C. Chueh, M. Liu, X. Li, W.-H. Chang, R. A. Kaindl, and C.-K. Shih, *Nano Lett.* **21**, 7363 (2021).
- [29] V. Dal Lago, M. Atala, and L. E. F. Foa Torres, *Phys. Rev. A* **92**, 023624 (2015).
- [30] S. Saha, S. N. Sivarajan, and D. Sen, *Phys. Rev. B* **95**, 174306 (2017).
- [31] Y. Yu, Y. Song, T. Chen, H. Wang, S. Zhuang, and Q. Cheng, *Chin. Opt. Lett.* **19**, 042601 (2021).
- [32] S. Bandyopadhyay, S. Bhattacharjee, and D. Sen, *J. Phys.: Condens. Matter* **33**, 393001 (2021).
- [33] H. Ammann, R. Gray, I. Shvarchuck, and N. Christensen, *Phys. Rev. Lett.* **80**, 4111 (1998).
- [34] P. H. Jones, M. M. Stocklin, G. Hur, and T. S. Monteiro, *Phys. Rev. Lett.* **93**, 223002 (2004).
- [35] I. Dana, E. Eisenberg, and N. Shnerb, *Phys. Rev. E* **54**, 5948 (1996).
- [36] L. Zhou and J. Gong, *Phys. Rev. A* **97**, 063603 (2018).
- [37] D. Y. H. Ho and J. Gong, *Phys. Rev. B* **90**, 195419 (2014).
- [38] M. Tashima, N. Hatano, *J. Phys. Soc. Jpn.* **82**, 113706 (2013).
- [39] R. Jafari, H. Johannesson, A. Langari, and M. A. Martin-Delgado, *Phys. Rev. B* **99**, 054302 (2019).
- [40] X. Qiao, X.-B. Zhang, Y. Jian, A.-X. Zhang, and J.-K. Xue, *Physica A* **576**, 126062 (2021).
- [41] J. H. Kang, J. H. Han, and Y. Shin, *New J. Phys.* **22**, 013023 (2020).
- [42] X. Li, E. Zhao, and W. V. Liu, *Nat. Commun.* **4**, 1523 (2013).
- [43] J. Zurita, C. Creffield, and G. Platero, *Adv. Quantum Technol.* **3**, 1900105 (2020).
- [44] J. Jünemann, A. Piga, S.-J. Ran, M. Lewenstein, M. Rizzi, and A. Bermudez, *Phys. Rev. X* **7**, 031057 (2017).
- [45] A. Altland and M. R. Zirnbauer, *Phys. Rev. B* **55**, 1142 (1997).
- [46] S. Mukherjee, A. Spracklen, D. Choudhury, N. Goldman, P. Öhberg, E. Andersson, and R. Thomson, *Phys. Rev. Lett.* **114**, 245504 (2015).
- [47] Y. Kuno, *Phys. Rev. B* **101**, 184112 (2020).
- [48] M. Di Liberto, S. Mukherjee, and N. Goldman, *Phys. Rev. A* **100**, 043829 (2019).
- [49] L. Li and S. Chen, *Phys. Rev. B* **92**, 085118 (2015).
- [50] T. L. Hughes, E. Prodan, and B. A. Bernevig, *Phys. Rev. B* **83**, 245132 (2011).
- [51] M. Grifoni and P. Hänggi, *Phys. Rep.* **304**, 229 (1998).
- [52] N. Goldman and J. Dalibard, *Phys. Rev. X* **4**, 031027 (2014).
- [53] S. Restrepo, J. Cerrillo, V. M. Bastidas, D. G. Angelakis, and T. Brandes, *Phys. Rev. Lett.* **117**, 250401 (2016).
- [54] S. Ryu, A. P. Schnyder, A. Furusaki, and A. W. Ludwig, *New J. Phys.* **12**, 065010 (2010).
- [55] R. Resta, *Rev. Mod. Phys.* **66**, 899 (1994).
- [56] D. Xiao, M.-C. Chang, and Q. Niu, *Rev. Mod. Phys.* **82**, 1959 (2010).
- [57] A. Eckardt and E. Anisimovas, *New J. Phys.* **17**, 093039 (2015).
- [58] H.-Y. Wang, L. Zhuang, X.-L. Gao, X.-D. Zhao, and W.-M. Liu, *J. Phys.: Condens. Matter* **32**, 355404 (2020).
- [59] M. Benito, A. Gómez-León, V. M. Bastidas, T. Brandes, and G. Platero, *Phys. Rev. B* **90**, 205127 (2014).
- [60] G. Dattoli, A. Torre, and S. Lorenzutta, *Matematiche* **53**, 387 (1998).
- [61] G. Dattoli, C. Chiccoli, S. Lorenzutta, G. Maino, M. Richetta, and A. Torre, *Nuovo Cimento B* **106**, 1159 (1991).
- [62] A. P. Schnyder, S. Ryu, A. Furusaki, and A. W. W. Ludwig, *Phys. Rev. B* **78**, 195125 (2008).
- [63] M. Suzuki, *Commun. Math. Phys.* **51**, 183 (1976).
- [64] R. Roy and F. Harper, *Phys. Rev. B* **96**, 155118 (2017).
- [65] J. K. Asbóth and H. Obuse, *Phys. Rev. B* **88**, 121406(R) (2013).
- [66] M. Thakurathi, A. A. Patel, D. Sen, and A. Dutta, *Phys. Rev. B* **88**, 155133 (2013).
- [67] P. Morigini, W. Chen, and R. Chitra, *Phys. Rev. B* **98**, 125129 (2018).
- [68] J. K. Asbóth, B. Tarasinski, and P. Delplace, *Phys. Rev. B* **90**, 125143 (2014).
- [69] L. Zhou and Q. Du, *Phys. Rev. A* **101**, 033607 (2020).
- [70] L. Zhou, *Entropy* **22**, 746 (2020).